Electromagnetic dipole strength of ^{136}Ba below the neutron separation energy

R. Massarczyk,[1] R. Schwengner,[1] F. Dönau,[1] E. Litvinova,[2] G. Rusev,[3,4,*] R. Beyer,[1] R. Hannaske,[1] A. R. Junghans,[1] M. Kempe,[1] J. H. Kelley,[4,5] T. Kögler,[1] K. Kosev,[1,†] E. Kwan,[3,4,‡] M. Marta,[1,§] A. Matic,[1,‖] C. Nair,[1,¶] R. Raut,[3,4,**] K. D. Schilling,[1] G. Schramm,[1,6] D. Stach,[1] A. P. Tonchev,[3,4,‡] W. Tornow,[3,4] E. Trompler,[1,††] A. Wagner,[1] and D. Yakorev[1]

[1]*Institut für Strahlenphysik, Helmholtz-Zentrum Dresden-Rossendorf, 01328 Dresden, Germany*

[2]*ExtreMe Matter Institute and Research Division, GSI Helmholtzzentrum für Schwerionenforschung, 64291 Darmstadt, Germany*

[3]*Duke University, Durham, North Carolina 27708, USA*

[4]*Triangle Universities Nuclear Laboratory, Durham, North Carolina 27708, USA*

[5]*Department of Physics, North Carolina State University, Raleigh, North Carolina 27695, USA*

[6]*Institut für Radiopharmazie, Helmholtz-Zentrum Dresden-Rossendorf, 01328 Dresden, Germany*

(Received 6 June 2012; published 17 July 2012)

The electromagnetic dipole strength of the nucleus ^{136}Ba has been investigated. Two measurements were performed with electron energies of 7.0 and 11.4 MeV at the bremsstrahlung facility at the ELBE accelerator of the Helmholtz-Zentrum Dresden-Rossendorf. Photon scattering experiments on the same nucleus have been performed at the high-intensity gamma-ray source (HIγS) facility of the Triangle Universities Nuclear Laboratory between 4.7 and 9.3 MeV. The GEANT4 code has been used to determine detector response and non-nuclear scattered events. Thus it is possible to account for the dipole strength in the quasicontinuum of unresolvable transitions. A statistical code was used to simulate inelastic transitions and to determine the branching ratios of transitions to the ground state. The resulting photoabsorption cross section is compared to quasiparticle random-phase approximation and relativistic quasiparticle time blocking approximation calculations.

DOI: 10.1103/PhysRevC.86.014319 PACS number(s): 25.20.Lj, 24.60.Dr, 26.50.+x, 27.60.+j

I. INTRODUCTION

The calculated production rate of various isotopes in astrophysical scenarios differs from the observed rates for many elements. For the different barium isotopes, there exists a discrepancy of up to 20% for the neutron capture cross sections [1]. These cross sections are an essential input for network codes calculating the abundances of elements. Below the neutron separation threshold, the different decay channels are determined by the level density and the photon-strength function (PSF), which can be described as the tail of the $E1$ giant dipole resonance (GDR). The PSF also has a large influence on the width of the different decay channels in a compound nucleus after neutron capture [2,3]. Neutron capture and photon scattering cross sections are also relevant for the microscopic simulation of radiation and neutron transport calculation for future transmutation facilities [4].

Various models are used to describe the shape of the GDR. The most common parametrization employs a single Lorentz curve (SLO) [5], as provided in the RIPL3 database [6]. Moreover, other descriptions exist, which take into account triaxial deformations, such as the triple Lorentzian model (TLO) [7]. Most of the models are fitted to data of (γ, n) experiments, but the energy region below neutron separation energy S_n is not described very well and differs remarkably from model to model. In addition, the so-called Pygmy dipole resonances (PDR) [8] have been found in many experiments during the last decade [9,10]. An enhanced strength below S_n could increase the reaction rate in astrophysical scenarios and change the predicted abundances [11,12].

In this article, we report on our measurements of the electromagnetic dipole strength of the even-even nucleus ^{136}Ba which was investigated at two different facilities. We performed experiments at the bremsstrahlung facility of the ELBE accelerator in Dresden-Rossendorf, Germany, and at the high-intensity gamma-ray source (HIγS) facility in Durham, North Carolina, USA. The ^{136}Ba nucleus has two neutron holes in the closed neutron shell at $N = 82$. Several experiments were performed in the past on $N = 82$ nuclides [9,13–15]. These studies investigated the strength below the neutron threshold and found extra strength; hence the question raised how nuclei beneath the neutron shell behave.

Previous studies on ^{136}Ba [16–18] have found several states in the range below excitation energies of $E_x \approx 4$ MeV. In contrast, the experiments at ELBE aimed at measuring the complete dipole response up to the neutron separation energy. In Sec. II, we give an overview on the experimental arrangements, whereas Sec. III describes the individual steps in the data analysis and the simulations performed. Finally in Sec. IV, we compare our results to predictions of a

*Present address: Chemistry Division, Los Alamos National Laboratory, Los Alamos, New Mexico 87545, USA.

†Present address: Bosch Solar Energy AG, 99310 Arnstadt, Germany.

‡Present address: Physics Division, Lawrence Livermore National Laboratory, Livermore, California 94550, USA.

§Present address: GSI Helmholtzzentrum für Schwerionenforschung, 64291 Darmstadt, Germany.

‖Present address: IBA Particle Therapy, 45157 Essen, Germany.

¶Present address: Nuclear Engineering Division, Argonne National Laboratory, Argonne, Illinois 60439, USA.

**Present address: UGC-DAE Consortium for Scientific Research, Kolkata Centre, Kolkata, India.

††Present address: ITC AG, 01067 Dresden, Germany.

quasiparticle random-phase approximation (QRPA) and relativistic quasiparticle time blocking approximation (RQTBA).

II. EXPERIMENTS

A. The bremsstrahlung facility at ELBE

At the superconducting electron linac ELBE of the Helmholtz-Center Dresden-Rossendorf bremsstrahlung is produced by electrons with energies up to 20 MeV hitting a thin niobium foil [19]. The electron momenta used for the present experiments were $p_e \cdot c = 11.4$ and 7.0 MeV. The first one ensured a sufficient photon flux up to the neutron separation energy of ^{136}Ba at $S_n = 9.107$ MeV. The second measurement at lower energy was used to identify inelastic transitions from excited nuclear levels to lower-lying levels.

Before entering a collimator, the bremsstrahlung photons produced pass through an aluminum hardener to reduce the number of low-energy photons. The photon energy distribution at the target position is plotted in Fig. 1. The total flux can be normalized by using well-known scattering cross sections of transitions in ^{11}B [20,21]. These transitions were corrected for branching and feeding and agree very well with the trend, which is explained in Sec. III E.

The amount of ^{11}B in the target was 318.1 mg. The target itself was a compound of $BaCO_3$ with a total mass of 2381.89 mg and an enrichment of 93% in ^{136}Ba.

The experimental setup consisted of four 100% high-purity Germanium (HPGe) detectors. Two were positioned at 90° and two at 127° relative to the beam axis. This allowed a determination of the multipole character of the observed transitions. Each detector was surrounded by an escape-suppression shield of bismuth germanate (BGO) which works as a veto detector, increasing the ratio of full energy events relative to all events. Lead collimators, each 10-cm thick, were placed in front of the detectors. The resulting spectra after 145 h of beam time with $p_e \cdot c = 11.4$ MeV are shown in Fig. 2. Strong transitions and a large continuum increasing toward low energies are clearly visible. The analysis of these data will be discussed in Sec. III.

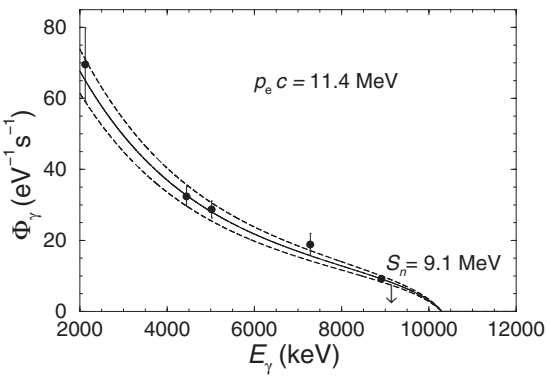

FIG. 1. Photon flux determined from the known integrated scattering cross sections of states in ^{11}B (circles) in comparison with the flux distribution explained in Sec. III E (black curve) and its uncertainties (dashed curves).

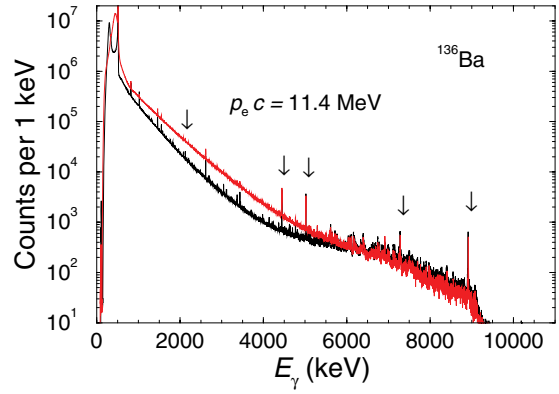

FIG. 2. (Color online) The measured spectra of ^{136}Ba after six days of beam time with $p_e \cdot c = 11.4$ MeV summed over the detector pair at 127° (black curve) and 90° (red curve). The arrows indicate the known transitions of ^{11}B.

B. The HIγS facility

The same target used at ELBE was studied at the high-intensity gamma-ray source (HIγS) facility [22] of the Triangle Universities Nuclear Laboratory. A high-intensity free-electron laser (FEL) is operated using electrons from the Duke University storage ring. The HIγS facility uses intracavity backscattering of polarized FEL photons in order to produce highly energetic photons up to 100 MeV. The polarization (linear or circular) is conserved in Compton scattering and leads to the production of photon beams with a degree of polarization of nearly 100%.

Four 60% HPGe detectors were placed around the target position at a polar angle of 90°. Two of them were placed in the horizontal plane, and the other two were placed in the vertical plane. This configuration in combination with the linearly polarized beam allowed us to distinguish between $M1$ and $E1$ transitions.

The γ rays produced at HIγS are monoenergetic and collimated for an energy spread of about 4% of the incident beam energy which allows us to scan over the whole energy range to test single transitions for their parity. This method has also the advantage, when compared to normal bremsstrahlung experiments, that the states within the adjusted energy bin are not fed from higher levels, which usually complicates the measurement. For our experiment, photon beam energies of E_γ = 4.7, 5.1, 5.6, 6.1, 6.5, 7.0, 7.5, 8.0, 8.4, 8.7, 9.0, and 9.3 MeV were used, where each energy was measured for 8 h.

III. DATA ANALYSIS

A. Resolved transitions

The first step in the analysis of the data from the experiment at ELBE was the assignment of energy levels to ^{136}Ba. As mentioned before, a second measurement at lower electron-beam energy was performed to identify transitions feeding low-lying states from states at higher energy. Shown in Fig. 3 are ratios of integrated scattering cross sections for intense transitions as deduced from the spectra measured at 11.4- and 7.0-MeV electron energy. Low-lying states exhibit a large

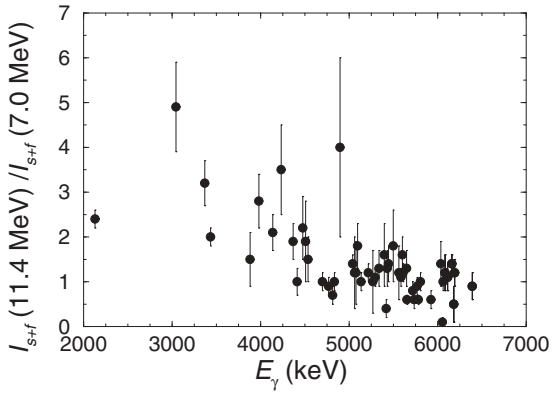

FIG. 3. Ratio of the integrated scattering cross sections of resolved states plotted for the two experiments at ELBE with different end points in photon energy.

ratio due to feeding from states above 7.0 MeV. For levels above about 5 MeV the ratios approach unity which indicates negligible feeding from higher-lying states.

The multipole order of transitions was determined from the ratios of intensities measured at 90 and 127° [23]. The expected ratios are 0.74 for $E1$ or $M1$ transitions, starting from the 0^+ ground state to an excited state with $J = 1^-$ or 1^+ and de-exciting back to the 0^+ state ($0 \to 1 \to 0$). For quadrupole transitions ($0 \to 2 \to 0$) this ratio is 2.28 including a correction for the opening angles of the detectors. If we assume a de-excitation via one or more intermediate states and feeding from above, this ratio approaches unity. In Fig. 4 the ratios of intensities measured with the two detector pairs show only a few quadrupole transitions and many transitions close to the theoretical value for dipole transitions.

Under polarized radiation at HIγS, the parity for most of the levels shown in Table I was measured. Also the spin value was cross checked. Figure 4 shows that the possibility to assign the spin of a level is limited at ELBE due to the feeding from above. Therefore we used the results from HIγS to assign also the spin. Unfortunately, some of the energy bins at chosen photon

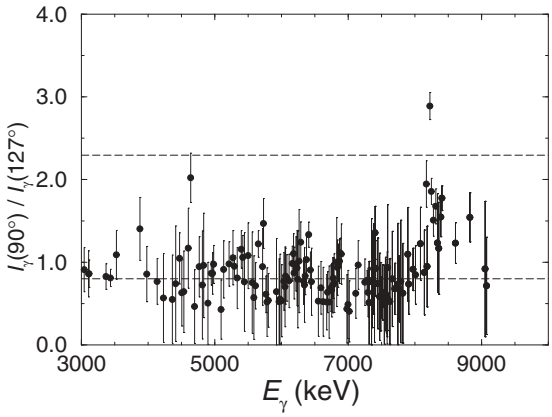

FIG. 4. Ratios of the intensities of transitions observed in the spectrum in the measurement with $p_e \cdot c = 11.4$ MeV at ELBE. Ratios around the expected value of 0.74 (dashed line) are assumed to have dipole character; those close to 2.28 to have quadrupole character.

energies were not broad enough to cover the complete energy range. Therefore, it was not possible to determine the parity for all states. Among the identified levels, no $M1$ transitions have been observed. This indicates a negligibly small $M1$ contribution to the dipole strength.

The resulting energy of an excited state E_x is, in principle, not equal to the measured γ-ray energy E_γ. After emission, the photon has a small energy loss due to small recoil of the target nucleus with the mass M:

$$E_x = E_{\gamma'} + \frac{{E_{\gamma'}}^2}{2M_{\text{target}}c^2}. \quad (1)$$

The Doppler effect for a detector which is placed at the angle θ gives an additional energy shift:

$$E_{\gamma'} = E_\gamma \left(1 + \frac{E_\gamma}{M_{\text{target}}c^2} \cos\theta\right). \quad (2)$$

The correction is for the nucleus ^{136}Ba in the order of a few tenth of keV increasing to higher energies. For the light ^{11}B the effect is considerably larger and shifts the observed peak a few keV. The level energies given in Table I were obtained by applying these corrections to the measured transition energies.

B. Detector response and efficiency

An important point in the data analysis of the continuum γ-ray strength is the correction of the experimental data for detector response. The detector response includes γ rays which have not deposited their full energy inside the detector volume. The detector setup was implemented in a GEANT4 [24] simulation, including the four HPGe detectors, their BGO shields, the lead shielding, and the components of the beam line. To check the implementation of the geometry, test runs were performed. For this, we used GEANT4 version 4.9.3. including the Livermore Low-Energy package.

For low γ-ray energies, radioactive sources such as ^{60}Co and ^{137}Cs were used to check the results of the simulated detector response. For example, the good agreement between simulation and experiment is shown in Fig. 5. GEANT4 is capable of describing the energy deposition in the detector system fairly well. Small differences are seen below the full energy peaks, which contribute in total only in the subpercent range.

At higher energies, another possibility to confirm the correctness of the simulations exists, which uses the excitation and de-excitation of levels in light nuclei with a low-level density. An example is shown in Fig. 6. For $^{\text{nat}}$C, only a few excited states can be seen in a photon scattering experiment. The figure shows a comparison of the detector response in the experiment and simulation of the single state at 15.1 MeV. The simulated spectrum reproduces the single and double escape peaks as well as the detector response down to about 11 MeV. Below this energy, the influence of other transitions and of the non-nuclear scattered events increases. The comparison between GEANT3 and GEANT4 shows a good agreement except in the low-energy range. Considering the incomplete setup in the simulation (missing walls and beam dump) the low-energy part is not treated satisfactorily. Therefore,

TABLE I. Levels assigned to ^{136}Ba.

E_x [a] (keV)	$\frac{\dot{N}_\gamma(90^\circ)}{\dot{N}_\gamma(127^\circ)}$ [b]	$\frac{\dot{N}_{\gamma\parallel}-\dot{N}_{\gamma\perp}}{\dot{N}_{\gamma\parallel}+\dot{N}_{\gamma\perp}}$ [c]	J_x^π [d]	$\frac{I_{s+f}(11.4)}{I_{s+f}(7.0)}$ [e]	I_s [f] (eV b)	Γ_0^2/Γ [g] (meV)
818.2(2)	0.82(2)		2^+ [h]	38.7(65)		
1551.1(2)	0.97(6)		2^+ [h]	28.2(84)		
2079.9(1)	0.97(6)		2^+ [h]			
2128.8(1)	0.93(7)		2^+ [h]	2.4(2)		
2223.6(5)	0.66(14)		$(2)^+$ [h]			
2484.6(1)	0.94(11)		2^+ [h]			
2693.3(2)	1.1(3)		1^+ [h]			
2773.0(1)	1.15(19)		2^+ [h]			
2779.3(8)	1.5(6)		2^+ [h]			
2976.7(6)	1.03(28)		2^+ [h]		18(3)	14(2)
3043.7(1)	0.91(16)		1^- [h]	4.9(10)	15(3)	59(7)
3109.9(1)	0.86(15)		2^+ [h]		32(5)	27(4)
3115.7(1)	0.86(9)		2^+ [h]		57(6)	48(5)
3369.6(1)	0.83(8)		$1^{(-)}$ [h]	3.2(5)	20(4)	62(6)
3435.1(1)	0.81(5)		1 [h]	2.0(2)	107(9)	109(9)
3526.0(3)	1.09(26)		2^+ [h]		15(2)	16(2)
3881.1(11)	1.4(5)			1.5(6)	10(2) [i]	13(3)
3979.8(2)	0.86(19)		(1)	2.8(6)	18(3) [i]	42(5)
4137.1(1)	0.77(12)		1	2.1(4)	19(3) [i]	59(6)
4231.2(2)	0.57(19)		1	3.5(10)	25(3) [i]	39(5)
4366.8(2)	0.55(11)		1	1.9(4)	18(3) [i]	56(9)
4413.3(1)	0.7(4)		(1)	1.0(3)	21(6) [i]	35(10)
4475.2(1)	1.05(24)		(1)	2.2(7)	12(3) [i]	46(8)
4536.4(3)	0.64(15)		1	1.5(5)	27(4) [i]	48(7)
4601.1(2)	0.7(4)		(1)		26(6) [i]	48(10)
4623.7(3)	0.7(10)	0.97(11)	1^-		36(4)	66(7)
4639.7(10)	2.0(10)	0.98(6)	1^-		35(4)	64(7)
4697.8(1)	0.46(13)	0.98(9)	1^-	1.0(2)	25(3)	49(6)
4767.7(1)	0.95(27)	0.89(34)	1^-	0.9(2)	41(4)	81(8)
4814.1(1)	0.73(25)		1	0.7(2)	28(9) [i]	57(17)
4833.3(5)	1.00(5)			1.0(2)	13(7) [i]	27(13)
4897.8(16)	0.50(18)		1	4.0(20)	12(4) [i]	27(13)
4985.0(6)	0.97(19)	0.91(20)	1^-		49(4)	106(9)
5039.6(29)	0.17(6)	0.97(6)	1^-	1.4(2)	80(9)	177(20)
5060.8(2)	0.31(9)	0.79(16)	1^-	1.2(8)	60(7)	163(19)
5076.9(8)	0.30(8)	0.98(6)	1^-	1.2(7)	54(7)	147(17)
5094.5(7)	0.43(11)	0.99(4)	1^-	1.8(5)	55(6)	223(24)
5135.2(3)	0.91(20)	0.93(3)	1^-	1.0(2)	46(9)	105(20)
5216.3(2)	0.98(18)		(1)	1.2(2)	47(7) [i]	110(16)
5268.4(7)	1.05(26)		(1)	1.0(7)	21(4) [i]	51(9)
5294.3(1)	0.95(8)		1	1.1(2)	85(8) [i]	206(19)
5337.8(2)	0.81(17)		1	1.3(4)	39(7) [i]	111(17)
5396.5(7)	1.16(21)		(1)	1.6(7)	23(6) [i]	96(14)
5418.4(5)	1.06(21)		(1)	0.4(2)	12(3) [i]	89(13)
5431.5(10)	0.52(22)		1	1.3(4)	34(4) [i]	70(12)
5444.4(1)	0.76(25)		(1)	1.4(4)	19(6) [i]	67(12)
5497.6(7)	1.1(4)	0.91(10)	1^-	1.8(8)	51(6)	133(15)
5561.1(3)	0.64(15)	0.97(9)	1^-	1.2(6)	25(4)	67(11)
5585.6(7)	0.81(8)	0.96(4)	1^-	1.1(2)	62(6)	167(17)
5601.2(1)	0.66(6)	0.99(3)	1^-	1.6(4)	44(11)	209(21)
5610.0(6)	0.9(3)	0.97(3)	1^-	1.2(2)	138(16)	328(29)
5647.9(13)	0.5(1)	0.99(3)	1^-	1.3(4)	62(10)	209(24)
5652.2(10)	1.22(13)	0.94(2)	1^-	0.6(1)	71(8)	198(23)

TABLE I. (*Continued*.)

E_x[a] (keV)	$\frac{\dot{N}_\gamma(90^\circ)}{\dot{N}_\gamma(127^\circ)}$[b]	$\frac{\dot{N}_{\gamma\parallel}-\dot{N}_{\gamma\perp}}{\dot{N}_{\gamma\parallel}+\dot{N}_{\gamma\perp}}$[c]	J_x^π[d]	$\frac{I_{s+f}(11.4)}{I_{s+f}(7.0)}$[e]	I_s[f] (eV b)	Γ_0^2/Γ[g] (meV)
5718(3)	1.0(4)		(1)	0.8(2)	94(9)[i]	268(26)
5735.0(7)	1.5(11)			0.6(2)	60(7)[i]	205(21)
5768.0(4)	0.61(9)		1	0.9(2)	90(9)[i]	259(25)
5781.7(9)	0.52(7)		1	0.6(1)	50(6)[i]	144(17)
5805.1(1)	0.54(10)		1	1.0(2)	48(10)[i]	181(19)
5924.2(6)	0.64(20)		1	0.6(2)	30(6)[i]	91(18)
5965.8(4)	0.52(19)	0.85(19)	1^-		31(6)	94(19)
5979.2(2)	0.55(20)	0.88(12)	1^-		24(6)	76(18)
6005.0(1)	0.53(11)	0.98(8)	1^-		38(7)	118(22)
6035.7(1)	0.77(16)	0.94(4)	1^-	1.4(5)	59(8)	279(50)
6052.9(2)	0.70(16)	0.98(4)	1^-	0.1(1)	71(15)	225(48)
6061.4(1)	0.83(16)	0.98(3)	1^-	1.0(2)	81(15)	258(48)
6082.5(1)	0.81(14)	0.99(2)	1^-	1.2(4)	97(29)	404(64)
6113.3(2)	0.78(13)	0.99(3)	1^-	1.1(3)	116(20)	441(77)
6161.2(2)	0.98(16)	0.98(4)	1^-	1.4(2)	92(15)	446(73)
6182.4(2)	0.83(20)	0.97(11)	1^-	0.5(4)	102(20)	375(81)
6192.8(8)	0.87(19)		(1)	1.2(3)	66(16)[i]	275(54)
6215.7(5)	0.98(26)		(1)		57(13)[i]	191(42)
6231.6(4)	0.9(3)		(1)		38(10)[i]	130(34)
6244.2(8)	0.8(3)		(1)		36(9)[i]	120(31)
6264.8(2)	1.0(4)		(1)		23(8)[i]	77(26)
6289.2(7)	1.24(27)		(1)		31(6)[i]	107(21)
6331.9(4)	0.77(16)	0.98(7)	1^-		107(14)	371(47)
6344.4(7)	0.72(12)	0.94(13)	1^-		68(11)	237(38)
6358.2(7)	0.83(13)	0.93(10)	1^-		112(13)	392(47)
6373.6(8)	1.0(7)	0.79(19)	1^-		58(10)	204(35)
6391.3(16)	0.8(1)	1.00(2)	1^-	0.9(3)	199(40)	815(87)
6409.9(19)	0.6(3)	0.99(3)	1^-		102(16)	364(55)
6430.6(11)	0.91(18)	0.99(4)	1^-		88(11)	316(39)
6449.5(2)	0.76(27)	0.93(7)	1^-		60(10)	215(35)
6478.2(1)	0.35(20)	0.97(14)	1^-		48(12)	176(44)
6488.7(1)	0.35(19)	0.90(12)	1^-		37(17)	137(62)
6528.8(11)	0.55(17)	0.95(15)	1^-		34(8)	124(31)
6554.3(8)	0.53(10)	0.75(24)	1^-		60(9)	223(35)
6591.8(3)	0.69(11)	0.92(26)	1^-		81(10)	304(38)
6625.3(1)	0.52(6)	0.91(28)	1^-		132(16)	503(61)
6677.3(3)	0.52(6)		1		101(12)[i]	392(47)
6693.4(1)	0.64(8)		1		110(13)[i]	428(51)
6716.8(3)	0.52(9)		1		85(13)[i]	334(51)
6741.9(3)	0.69(10)	0.98(3)	1^-		118(13)	466(52)
6756.6(2)	0.66(11)	0.76(14)	1^-		69(8)	273(32)
6767.8(1)	0.72(11)	0.89(12)	1^-		45(6)	180(23)
6776.8(1)	0.81(14)	0.74(19)	1^-		69(8)	275(32)
6788.4(2)	0.75(24)	0.76(16)	1^-		51(7)	205(28)
6830.8(7)	1.00(29)	0.76(22)	1^-		23(6)	92(23)
6840.3(8)	0.94(18)	0.97(3)	1^-		51(9)	205(35)
6847.5(11)	0.96(17)	0.96(5)	1^-		68(10)	277(42)
6859.2(8)	0.99(18)	0.90(8)	1^-		61(7)	250(30)
6870.4(10)	1.01(16)	0.85(15)	1^-		46(6)	189(26)
6880.5(5)	1.11(28)	0.85(7)	1^-		65(8)	267(31)
6895.8(2)	1.10(19)	0.74(12)	1^-		28(5)	114(21)
6952.0(11)	0.46(13)	0.94(3)	1^-		40(11)	169(47)
6982.3(2)	0.44(7)	0.97(3)	1^-		131(15)	555(64)

TABLE I. (*Continued.*)

E_x[a] (keV)	$\frac{\dot{N}_\gamma(90^\circ)}{\dot{N}_\gamma(127^\circ)}$[b]	$\frac{\dot{N}_{\gamma\parallel}-\dot{N}_{\gamma\perp}}{\dot{N}_{\gamma\parallel}+\dot{N}_{\gamma\perp}}$[c]	J_x^π[d]	$\frac{I_{s+f}(11.4)}{I_{s+f}(7.0)}$[e]	I_s[f] (eV b)	Γ_0^2/Γ[g] (meV)
6998.5(7)	0.49(15)	0.97(1)	1^-		91(24)	385(101)
7006.6(14)	0.41(13)	0.99(1)	1^-		77(22)	327(94)
7018.9(1)	0.41(7)	0.97(2)	1^-		99(13)	421(56)
7150.6(1)	0.97(22)		(1)		71(15)[i]	315(68)
7251.1(3)	0.76(17)	0.83(16)	1^-		85(11)	387(52)
7271.6(5)	0.47(8)	0.77(26)	1^-		52(10)	240(43)
7281.5(15)	0.72(8)	0.76(25)	1^-		356(32)	1635(145)
7298.8(1)	0.64(11)	0.83(14)	1^-		92(11)	427(50)
7314.8(2)	0.51(22)	0.97(13)	1^-		71(10)	327(44)
7350.2(14)	0.76(29)	0.90(26)	1^-		38(7)	176(31)
7364.1(3)	0.8(3)	0.98(9)	1^-		68(8)	320(39)
7382.1(4)	0.9(4)	0.98(6)	1^-		54(8)	256(36)
7394.4(9)	0.74(23)	0.9(4)	1^-		52(9)	244(43)
7402.5(3)	1.4(4)	0.96(6)	1^-		47(9)	222(40)
7414.9(13)	0.93(27)	0.96(18)	1^-		59(8)	279(38)
7444.4(3)	0.74(16)	0.98(3)	1^-		70(12)	336(55)
7472.5(1)	0.58(11)	0.98(3)	1^-		74(12)	358(58)
7487.5(4)	0.58(8)	0.99(3)	1^-		92(13)	447(61)
7502.8(3)	0.58(7)	0.99(1)	1^-		178(18)	875(90)
7519.2(10)	0.64(12)	0.95(4)	1^-		87(11)	424(54)
7541.0(6)	0.49(9)	0.88(9)	1^-		71(10)	351(50)
7558.1(7)	0.62(11)	0.98(5)	1^-		68(10)	336(51)
7572.1(1)	0.56(12)	0.98(7)	1^-		104(14)	516(69)
7583.5(8)	0.57(24)	0.97(10)	1^-		65(14)	324(71)
7594.8(5)	0.9(11)	0.9(5)	1^-		38(13)	190(65)
7604.2(8)	0.25(7)		1		47(16)[i]	237(58)
7625.7(4)	0.52(14)		1		74(11)[i]	371(53)
7662.3(2)	0.8(6)		1		38(9)[i]	192(45)
7675.6(2)	0.40(14)		1		24(8)[i]	121(41)
7699.0(3)	0.68(20)		1		1110(14)[i]	563(71)
7747.6(5)	0.74(22)		1		32(9)[i]	168(47)
7769.8(1)	0.68(22)		1		85(13)[i]	445(68)
7788.1(5)	0.77(26)		(1)		31(9)[i]	164(46)
7819.8(8)	0.63(20)	0.90(10)	1^-		47(9)	247(48)
7848.9(3)	0.4(4)	0.97(10)	1^-		58(16)	309(85)
7857.9(12)	0.22(10)	0.97(3)	1^-		45(13)	239(68)
7875.0(11)	0.30(12)	0.97(3)	1^-		48(15)	258(80)
7895.2(2)	1.1(5)	0.99(5)	1^-		44(17)	235(92)
7911.3(4)	0.73(13)	0.98(2)	1^-		155(25)	846(135)
7972.4(10)	0.91(18)	0.99(2)	1^-		89(14)	490(75)
8006.6(5)	0.85(24)	0.98(2)	1^-		63(11)	347(61)
8083.5(3)	1.2(9)	0.99(4)	1^-		20(6)	112(35)
8124.7(2)	0.57(25)	0.7(6)	1^-		10(4)	56(21)
8144.3(7)	0.88(26)	0.7(5)	1^-		19(4)	110(24)
8171.2(10)	2.0(8)	0.9(4)	1^-			
8184.3(3)	0.95(29)	0.7(5)	1^-		18(4)	102(24)
8227.9(5)	2.9(8)	0.8(6)	1^-			
8250.8(7)	1.9(4)	0.93(23)	1^-			
8280.4(10)	1.5(3)	0.95(15)	1^-			
8315.4(9)	1.7(7)	0.94(20)	1^-			
8339.2(14)	1.2(6)	0.79(29)	1^-		18(6)	106(34)
8359.5(5)	1.2(3)	0.8(9)	1^-		23(6)	139(38)
8389.7(7)	1.6(4)	0.9(4)	1^-			

TABLE I. (*Continued.*)

E_x[a] (keV)	$\frac{\dot{N}_\gamma(90^\circ)}{\dot{N}_\gamma(127^\circ)}$[b]	$\frac{\dot{N}_{\gamma\parallel}-\dot{N}_{\gamma\perp}}{\dot{N}_{\gamma\parallel}+\dot{N}_{\gamma\perp}}$[c]	J_x^π[d]	$\frac{I_{s+f}(11.4)}{I_{s+f}(7.0)}$[e]	I_s[f] (eV b)	Γ_0^2/Γ[g] (meV)
8404.1(13)	1.8(4)	0.9(5)	1^-			
8611.1(21)	1.23(29)	0.95(16)	1^-		66(16)	427(100)
8825.1(10)	1.5(7)	0.83(17)	1^-			
9049.5(7)	0.9(5)	0.9(3)	1^-		58(27)	414(192)
9077.8(7)	0.7(3)	0.92(16)	1^-		105(25)	747(180)

[a]Excitation energy. The error in parentheses is given in units of the last digit. This energy includes a recoil and Doppler-shift correction.
[b]Ratio of the rates of the ground-state transitions measured at angles of 90 and 127°.
[c]Azimuthal asymmetry of the ground-state transitions deduced from the scattering of polarized photons at HIγS.
[d]Spin and parity of the state.
[e]Ratio of integrated scattering + feeding cross sections deduced at the two measured electron energies.
[f]Integrated scattering cross section.
[g]Partial width of the ground-state transition Γ_0 multiplied with the branching ratio $b_0 = \Gamma_0/\Gamma$.
[h]Spin and parity known from other work (see Sec. I).
[i]Value deduced under the assumption of $J_x = 1$.

data below 2–3 MeV are excluded in the final cross-section evaluation.

The detector response was simulated over the entire energy range in 10-keV steps. Beginning with the bin at the highest energy, the normalized simulated spectrum below the full energy peaks was subtracted step by step from the experimental spectrum. In Fig. 7, one can clearly see for the ^{11}B transition at 8.9 MeV, marked by an arrow, how the single escape peak (SE) is removed from the spectrum, whereas the full energy peak (FE) remains unchanged.

The simulation of the detector response was also used to determine the efficiency, $\varepsilon(E)$, of the detector setup. This value can be measured directly at some energies with calibrated sources. Figure 8 shows the efficiency dependence over the energy range of the measurements. GEANT3 as well as GEANT4 are capable of describing the trend in the region of lower energies. At higher energies, the difference is negligibly small.

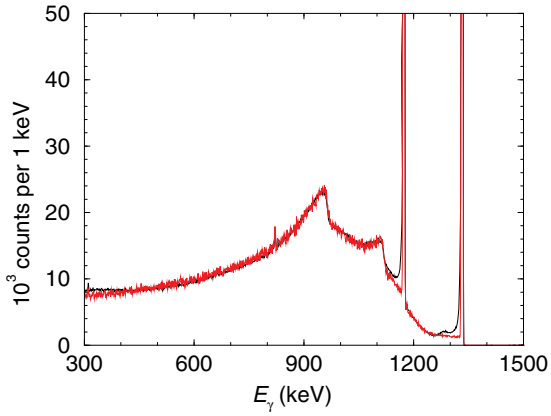

FIG. 5. (Color online) Comparison of the simulated and experimental detector response. Shown in the figure is the measured spectrum of a ^{60}Co source (black curve) and the simulation (red curve) under the same geometrical conditions. The simulation is normalized to the experimental counts in the full energy peak at 1332 keV.

The uncertainty of the efficiency was determined by fixing the simulated data to the absolute efficiency of a ^{137}Cs and a ^{60}Co source. Consequently, we estimated the uncertainty of the absolute efficiency values to be 5%.

C. Atomic background

In photon scattering experiments, photons do not only interact with the nuclei. In fact, the cross sections for interactions with the atomic electrons are about one or two orders of magnitude higher than the nuclear scattering at low energy. The first one is in the range of 10 to 20 b (data from NIST XCOM; see also Ref. [25]). The second one is in the range of a few mb, which should be in agreement with results of other experiments in this mass range (see Ref. [26]). In

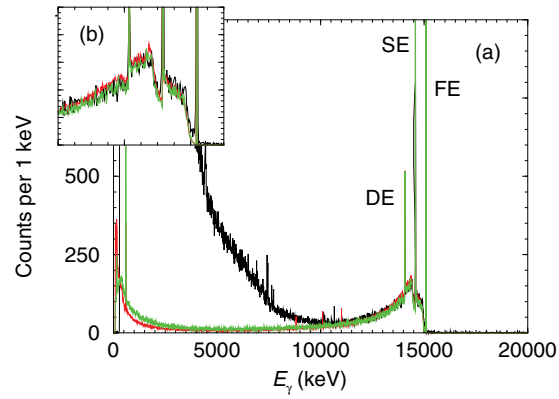

FIG. 6. (Color online) (a) Spectrum of photons scattered from ^{nat}C (black curve) in comparison with the simulations with GEANT3 (green curve) and GEANT4 (red curve). The simulations reproduce the single escape peak (SE) as well as the double escape peak (DE), when fitting the simulated area of the full energy peak (FE) to the experimental one. (b) A closer look at the energy region below the 15.1-MeV peak.

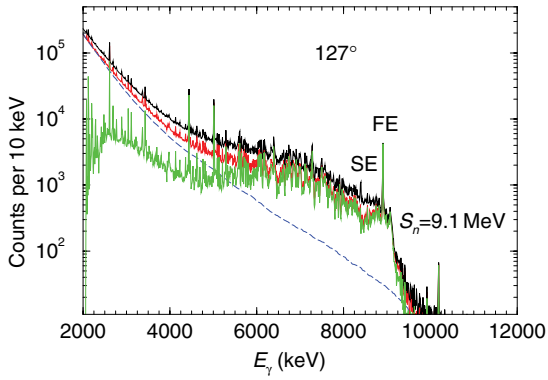

FIG. 7. (Color online) Spectrum summed for detectors at 127° in the different steps of data analysis. The original spectrum, natural background removed (black curve), is corrected for detector response (red curve). The simulated non-nuclear scattered events (blue dashed curve) simulated with GEANT4 have to be subtracted from this. The final spectrum (green) includes only γ rays from nuclear transitions. The abbreviations FE and SE denote the full energy peak and the single escape peak of the ^{11}B transition at 8.9 MeV, as described in Sec. III B.

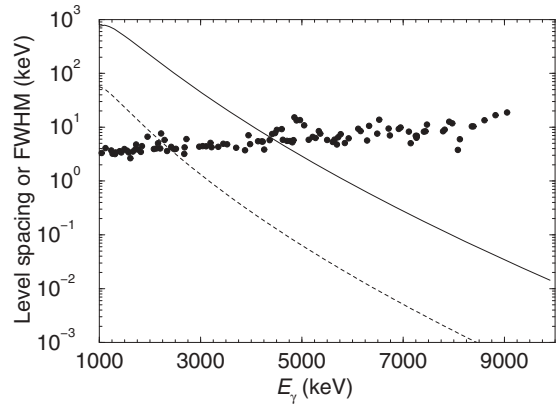

FIG. 9. Comparison of detector resolution and level spacing. The dots show the full width at half maximum (FWHM) of the observed transitions. The solid curve shows the average level spacing, predicted by the back-shifted Fermi-gas model (BSFG) as mentioned in Sec. III D just for $J^\pi = 1^-$ states. The dashed curve is the average level spacing in the BSFG model including all spins and parities.

principle, the atomic background at the detector position can be divided into different types:

(1) Events which result from only one scattering in the target can be the photons, which have only small energies left ($E_\gamma \leqslant 1$ MeV) when hitting a detector under backward angles after Compton scattering in the target.

(2) Further events are processes involving two or more steps. There could be a pair production inside of the target. The positron then will annihilate and produces 0.511-MeV γ rays or the electron from this process can be stopped or lose energy by emitting photons. For higher photon energies in the background, it can be verified with the help of GEANT4 that these are mainly bremsstrahlung photons. This radiation is generated when the primary photons produce high-energy electrons via Compton scattering inside the target.

(3) Other sources of radiation can be due to the scattering of secondary particles in the detector setup and at the beam tube. Because the setup is constructed for low background conditions (minimum of construction material, large room, etc.; see [19]), these events are considered to have a minor influence on the spectra.

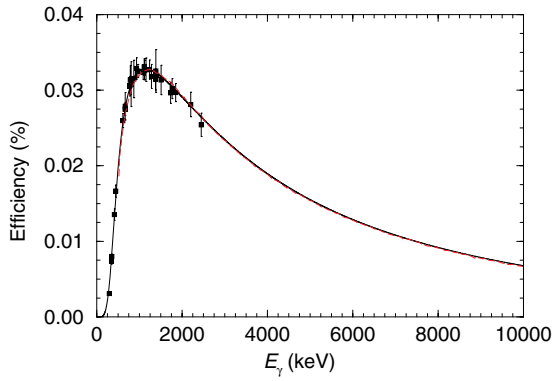

FIG. 8. (Color online) Absolute detector efficiency obtained from calibration standards (data points) and from simulations with GEANT3 (black curve) and GEANT4 (red dashed curve) for one detector at 127°.

Figure 7 shows the comparison between the measured spectrum—that has been corrected for natural background, detector efficiency, and response—and the spectrum caused by atomic processes. The so-called atomic background fits well at the low-energy part of the experimental spectrum, as well as at the high energies above the neutron separation threshold, where we expect no more nuclear scattered photons due to the open (γ, n) channel and decreasing (γ, γ') channel.

As a result, we obtain a large continuum of events at all photon energies up to the neutron separation energy after subtracting of the non-nuclear scattered events. This continuum can be explained by the increasing level density and the finite detector resolution. As can be seen in Fig. 9 at an energy of about 4–5 MeV, the resolution of the germanium detector is worse than the average level spacing in ^{136}Ba and only very intense peaks will tower out in the continuum.

In order to get full information about the dipole response and the photoabsorption cross section, one has to include this continuum of unresolved peaks. As previous work [13,27–30] has shown, the intensity of the continuum can be in the range of about two thirds of the total intensity.

D. Correction for inelastic transitions

An excited state i at an energy E_i does not need to decay to the ground state directly. It can decay to all states f with a lower energy $E_f < E_i$. For each linking transition, a transition width Γ_{if} exists. The probability for the decay of state i to state f is

$$p_{i\to f} = \frac{\Gamma_{if}}{\Gamma_i}, \quad \text{with} \quad \Gamma_i = \sum_f \Gamma_{\text{if}}. \tag{3}$$

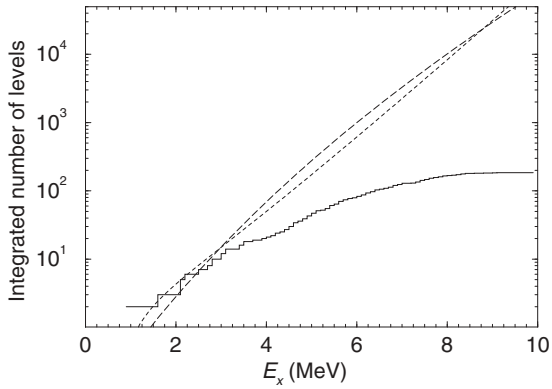

FIG. 10. Integrated level density in experiment and model. The stairs show the experimental number of levels up to a certain energy bin. BSFG model (dashed line) and constant-temperature model (dotted curve) describe the low-energy part and the region around S_n [33], but no assertion can be made about which model should be preferred, due to the finite detector resolution.

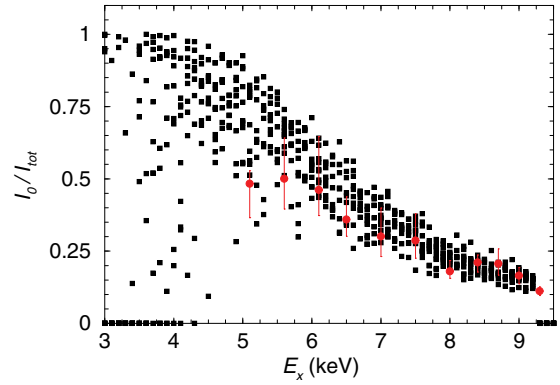

FIG. 11. (Color online) Simulated ratio of the intensity of ground-state transitions to the intensity for all transitions of levels in a given bin for ten realizations (black squares) in comparison to experimental values obtained from the experiment at HIγS (red circles).

It is known [31] that an average radiative width for transitions between two states can be described by

$$\langle \Gamma_{if} \rangle = \frac{f_{XL}(E_\gamma) {E_\gamma}^{2L+1}}{\varrho(E_f, J_f)}, \tag{4}$$

where XL is the multipolarity of the transition. The quantity$\varrho(E_f, J_f)$ is the density of states with spin J_f at an energy E_f. Transition energy E_γ is the difference of the energies of the states $E_i - E_f$ and $f_{XL}(E_\gamma)$ is the strength function, which depends only on E_γ, according to the Axel-Brink hypothesis [5,32].

Unfortunately, most of these quantities are not known exactly or they fluctuate. Therefore, we have to make the following assumptions:

(1) The photoabsorption cross section will be given in certain energy bins. In one bin, the number of levels is large enough to justify a statistical treatment. This supposition is not valid for lower energies ($E_x \lesssim 4$ MeV).

(2) Due to the incomplete information about level density, one has to assume a model. In previous work [13,27–30], the backshifted Fermi-gas (BSFG) model was used. To have comparable results we also employed the BSFG model in this analysis. The parameters used for ^{136}Ba are $a = 12.34(28)$ MeV^{-1} and $E_1 = 0.83(14)$ MeV, according to Ref. [33]. In Fig. 10, BSFG predictions are shown in comparison to experimental data and the values predicted by the constant-temperature model. In addition to this, one has to assume a spin distribution, which was also taken from Ref. [33]. We assume that positive and negative parities are distributed equally, which is a reasonable assumption for excitation energies above 4 MeV, according to Ref. [34].

(3) One has to choose a model for the different strength functions. For the $E1$ strength, one could use a simple model like the description with one or two Lorentzian functions as given in RIPL3 [6]. A more general model is the triple Lorentzian model [7], which uses a combination of three Lorentzian curves. The parameters of this model are based on a global fit for medium-mass and heavy nuclei and thus the model is useful for the description of the electric-dipole strength function in nuclei for which (γ, n) cross sections have not been measured. The various models for ^{136}Ba differ in the low-energy region. A single Lorentz curve was used with the parameters deduced from experimental data for the neighboring isotope ^{138}Ba and given in RIPL3 [6]: $\Gamma = 4.6$ MeV for the width of the Lorentzian, $E_r = 15.25$ MeV for the resonance energy of the GDR, and $\sigma = 325.8$ mb for the peak cross section.

(4) $M1$ and $E2$ transitions are also taken into account. Their strength functions are parametrized relative to the $E1$ strength function, as recommended in RIPL3.

(5) It is only possible to calculate averaged transition widths. The partial width of a transition varies according to a Porter-Thomas distribution [35].

In practice, one generates a level scheme, in which the levels are distributed according to the level density mentioned above. The average transition widths are calculated using Eq. (4) and varied according to a Porter-Thomas distribution. Each of these so-called realizations is excited many times and the decay spectra are recorded. One of these realizations cannot represent the nucleus exactly. Therefore, 1000 different randomized level schemes were built. In Fig. 11 branching ratios of ground-state transitions for various excitation energies in ten realizations are compared with experimental values derived from the HIγS measurement. For this purpose the HIγS spectra were corrected for natural background and detector response, efficiency, and atomic background. These steps are shown in Fig. 12. After subtraction, one can clearly see the transitions to the ground state and to other states. For higher excitation energies, the intensities of the transitions to the first excited state are very small. A cutoff for energies below 600 keV was used in the data analysis, because it was not possible to estimate the complete room background caused by scattered photons.

The experimental values are in good agreement to the simulated ones. The large error bars result from the difficult estimate of the total photon flux on the target in a given energy bin. The simulated atomic background has to be normalized to this experimental value. For this experiment, we calculated

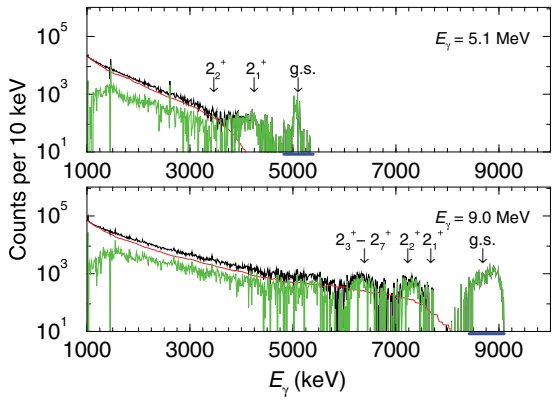

FIG. 12. (Color online) Spectra from the experiment at HIγS. The plots show the response-corrected spectra (black) for two different beam energies. After removing the simulated non-nuclear scattered events (red), the resulting spectra (green) show the groups of transitions to the ground state (g.s.) and to excited states (2_1^+, 2_2^+, ...). The blue lines below the energy axis show the energy spread of the incident photon beam.

the flux in a given energy bin at HIγS from intense transitions in the energy bin using the known flux at the ELBE facility. At some of the excitation energies, only a few small peaks appeared, which produced a large uncertainty.

In the spectra measured at ELBE, which were corrected for detector response, efficiency, and atomic background, the inelastic transitions are removed step by step starting from the highest excitation energies.

E. Calculation of the photoabsorption cross section

After performing all these steps we obtained a final spectrum, which consists of only full energy peaks representing the ground-state transitions with their real intensity. The following formula is used to calculate the integrated scattering cross section $I_s(E_x)$ relative to the one of a state in ^{11}B [20,21]:

$$\frac{I_s(E_x)}{I_s(E_x^{\mathrm{B}})} = \left[\frac{I_\gamma(E_\gamma,\theta)}{W(E_\gamma,\theta)\epsilon(E_\gamma,\theta)\Phi_\gamma(E_x)N_N}\right] \times \left[\frac{I_\gamma(E_\gamma^{\mathrm{B}},\theta)}{W^{\mathrm{B}}(E_\gamma^{\mathrm{B}},\theta)\epsilon(E_\gamma^{\mathrm{B}},\theta)\Phi_\gamma(E_x^{\mathrm{B}})N_N^{\mathrm{B}}}\right]^{-1}. \quad (5)$$

In this equation we have the following quantities:

(1) All quantities with index B refer to values of an excited state in ^{11}B which are known [$(I_s(E_x^{\mathrm{B}}), W(E_\gamma^{\mathrm{B}},\theta)$] or calculated [$I_\gamma(E_\gamma^{\mathrm{B}},\theta)$, $\epsilon(E_\gamma^{\mathrm{B}},\theta)$, $\Phi_\gamma(E_x^{\mathrm{B}})$]. In the calculation, the state at 8.921 MeV was used, because this level is not fed from higher-lying levels.

(2) $I_\gamma(E_\gamma,\theta)$ is the intensity for photons which are detected with energy E_γ. This energy can be transferred to the excitation energy E_x by taking into account the recoil of the nucleus and the Doppler shifting of the photons (see Sec. III A).

(3) $W(E_\gamma,\theta)$ is the angular correlation.

(4) $\Phi_\gamma(E_x)$ is the incident photon flux as shown in Fig. 1. The distribution is calculated by using the formula given in Ref. [36] which is used as an input in GEANT4 simulation. This simulation is used to determine the change of the photon spectrum by the aluminum hardener. The absolute height of the curve is adjusted to the flux values deduced at the levels of ^{11}B. The curve is fitted to the data points at 4.444, 5.020, and 8.921 MeV. The data point at 7.285 MeV is not used in the fit, because other experiments [13,27] have shown that this value may be overestimated. The data point at 2.125 MeV has a large uncertainty because of the correction performed for feeding from the other states. Therefore, this value is not used for the flux determination, although it agrees well with the fitted curve.

(5) $\epsilon(E_\gamma,\theta)$ is the efficiency for one detector at a certain angle θ as mentioned in Sec. III B. The trend of the efficiency as a function of energy can be seen in Fig. 8.

(6) N_N gives the number of atoms of ^{136}Ba and ^{11}B.

The integrated scattering cross section is calculated for single transitions as well as for complete energy bins of 100-keV width. The values for single transitions to the ground state are listed in Table I. These data can be used to calculate the ratio of Γ_0^2/Γ with the following formula:

$$I_s = \int \sigma_{\gamma\gamma} dE = \left(\frac{\pi\hbar c}{E_x}\right)^2 \frac{2J_x+1}{2J_0+1}\frac{\Gamma_0^2}{\Gamma}. \quad (6)$$

Here, $\sigma_{\gamma\gamma}$ is the elastic scattering cross section. E_x is the excitation energy of the level. J_x and J_0 are the spins of the excited level and the ground state, respectively.

The values of I_s deduced for resolved transitions are strongly influenced by feeding from higher-lying states and the measured scattering cross section contains two contributions; $I_{s+f} = I_{\mathrm{scattering}} + I_{\mathrm{feeding}}$, $I_{\mathrm{scattering}}$ from the direct excitation, and I_{feeding} from feeding from higher-lying states. The two parts cannot be disentangled by using the statistical simulations of γ-ray cascades, because the transition widths between two particular levels cannot be determined accurately as they undergo variations according to the Porter-Thomas distribution (see Sec. III D).

The photoabsorption cross sections σ_γ were calculated for each of the nuclear realizations using the ground-state branching ratios described in Sec. III D:

$$\sigma_\gamma = \sigma_{\gamma\gamma}\left(\frac{\Gamma_0}{\Gamma}\right)^{-1}. \quad (7)$$

Subsequently, average cross sections were deduced for each energy bin.

IV. RESULTS

A. Experimental results

The distribution of the experimental photoabsorption cross section σ_γ of ^{136}Ba is shown in Fig. 13 in comparison with phenomenological approximations to the GDR. The experimental data display an enhancement over the phenomenological curves at excitation energies between 5.5 and 8.0 MeV that amounts to about 3.9% of the Thomas-Reiche-Kuhn sum rule [37].

In Fig. 14, the experimental photoabsorption cross section of ^{136}Ba is compared with those of the two $N = 82$ neighbors

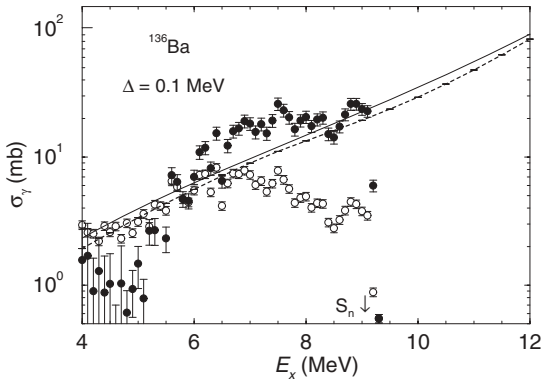

FIG. 13. Photoabsorption cross section in ^{136}Ba as a function of excitation energy. Open circles show the cross section without the correction for feeding and branching. The filled circles show the corrected absorption cross section. The solid curve represents a single Lorentz curve with the parameters given in the text, and the dashed curve shows the prediction of the TLO model.

^{138}Ba [14] and ^{139}La [13]. The cross section of ^{136}Ba is similar to that of ^{138}Ba. The enhancement of strength in the Ba isotopes is less distinctive than in the odd-mass neighbor ^{139}La.

B. QRPA calculations

As a first theoretical model to compare our data to, we use the quasiparticle random-phase approximation (QRPA), which is explained in detail in Ref. [40]. The nuclear shape of the ^{136}Ba is assumed to be spherical for the calculations. The calculations use the following Hamiltonian:

$$H_{E1}^{\mathrm{QRPA}} = h_{\mathrm{MF}} - \frac{1}{2}\sum_{t=0,1}\sum_{\mu=-1,+1}\kappa_{1\mu}^{t} Q_{1\mu}^{t} Q_{1-\mu}^{t} - \frac{1}{2}\sum_{t=0,1}\sum_{\mu=-3,+3}\kappa_{3\mu}^{t} Q_{3\mu}^{t} Q_{3-\mu}^{t}. \quad (8)$$

Here, h_{MF} stands for the quasiparticle Hamiltonian. It consists of a Woods-Saxon mean field and a monopole pair potential. By defining the multipole operators $Q_{\lambda\mu}^{t} = [r^{\lambda}Y_{\lambda\mu}]^{\pi} + (-1)^{t}[r^{\lambda}Y_{\lambda\mu}]^{\nu}$ the isoscalar ($t = 0$) and isovector ($t = 1$) parts of the dipole ($\lambda = 1$) and octupole ($\lambda = 3$) interaction are included. This part depends on the values $\kappa_{\lambda\mu}^{t=1}$ which are adjusted such that they reproduce the maximum of the GDR. The suppression of the spurious center-of-mass motion [41] allows us to calculate transition strengths. It is not necessary to assume an effective charge for the neutrons, so the bare proton charge e_π can be used. Then the transition operator is given by

$$\hat{M}(E1)_{\mu} = e_{\pi}\sum_{i=1}^{Z}[rY_{1\mu}]_i. \quad (9)$$

The resulting QRPA spectrum shown in Fig. 15 was obtained by folding the solutions with Lorentzians of a width of 250 keV.

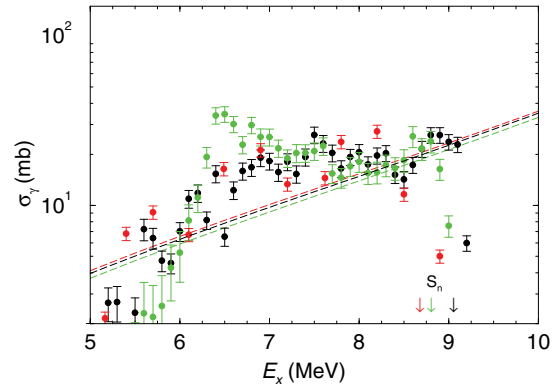

FIG. 14. (Color online) Comparison between different isotopes in the same mass region. The measurement of this work on the nucleus ^{136}Ba is represented by the black points. The strength function (black dashed curve) is given as a theoretical prediction. The green dots represent the measured photoabsorption cross section on ^{139}La [13] whereas the green dashed curve shows an SLO as fitted in the RIPL3 database to (γ, n) data on the same nucleus [38] corrected with a factor 0.85 [39]. The red circles [14] and the dashed curve [6] show the same information for the nucleus ^{138}Ba, respectively.

C. RQTBA calculations

The relativistic quasiparticle time blocking approximation (RQTBA) [42,43] for nuclear response is based on the covariant energy density-functional theory (CEDFT) with effective meson-exchange interaction. The CEDFT provides the working basis for further extensions beyond the mean-field approach. The nuclear response function is described by the Bethe-Salpeter equation (BSE) in the two-quasiparticle space with an energy-dependent two-quasiparticle residual interaction which is the exact variational derivative of the phonon coupling self-energy with respect to the one-body Green's function. The BSE is solved either in the basis of Dirac states, forming the self-consistent solution of the relativistic Hartree equations for the ground state, or in the momentum-

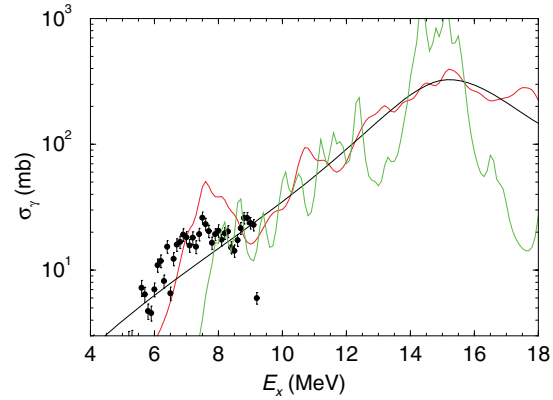

FIG. 15. (Color online) Experimental data (black circles) in comparison to an SLO curve (black curve), the results of the RQTBA calculation (red curve), and the QRPA calculation (green curve). All data sets are given in 100-keV bins, QRPA strength is smeared out with Lorentzian functions of 250-keV width, and RQTBA results are obtained with the imaginary part of the energy variable equal to 250 keV.

channel representation (see [42] for details). The approach is fully consistent: the same set of the coupling constants generates the Dirac-Hartree single-quasiparticle spectrum, the static part of the residual two-quasiparticle interaction, phonon spectra, and the quasiparticle-phonon coupling amplitudes. The RQTBA solution of the BSE generates excitation spectra with a multitude of 2q⊗phonon (two quasiparticles ⊗ phonon) states providing a fragmentation of the giant resonances and of the soft modes obtained in RQRPA. Thus, within the RQTBA the excited states are built of the two-quasiparticle-phonon (2q⊗phonon) [42] or two-phonon [43] configurations, so that the model space is constructed with the quasiparticles calculated within the relativistic mean field and the phonons computed within the self-consistent relativistic QRPA. The quasiparticle space is complete up to 100 MeV and phonons with natural parities and angular momenta up to $J = 6$ with energies below 15 MeV are included in the model space.

In this work, we present results obtained within the original version of the RQTBA [42]. To mimic missing complex configurations and the continuum above the particle threshold, the smearing parameter (imaginary part of the energy variable) was taken equal to 250 keV.

D. Comparison of experimental with calculated cross sections

The present experimental cross sections are compared with the QRPA and RQTBA predictions in Fig. 15. The calculated cross sections follow the general behavior of the GDR parametrization. The QRPA prediction shows large fluctuations in the GDR region, whereas the RQTBA prediction is more smooth as a result of the fragmentation of strength caused by the inclusion of 2q⊗phonon excitations. The QRPA calculations do not reproduce the experimental strength below about 7.5 MeV, whereas the fragmentation of strength in the RQTBA calculations brings strength toward low energy. The RQTBA calculations produce a prominent peak at about 8 MeV, somewhat above the experimental enhanced strength. In these calculations, there is a lack of strength at energies below about 6.5 MeV. This indicates that the model space of RQTBA is still not large enough to reproduce the lowest dipole excitations and higher-order correlations have to be included to cause further fragmentation.

V. CONCLUSIONS

The response of ^{136}Ba to dipole radiation was investigated. In total about 170 new levels have been observed. For most of them spin and parity assignments have been made by the combined information from ELBE and HIγS. A significant $M1$ contribution to the total strength has not been observed in the experiment with polarized γ rays.

It has been shown that it is possible to deduce photoabsorption cross sections at ELBE from the beginning of the statistical regime at about 4 MeV up to the neutron separation energy. A continuum analysis has been successfully performed which takes into account unresolved strength. The GEANT4 code has proven its ability to describe the response of our detector system. Also the influence of non-nuclear scattered events can be estimated. The results of the statistical treatment in a code used for the determination of elastic and inelastic scattering at ELBE have been verified by the experimental measured intensities at HIγS. As a result of the present study, an enhancement of the dipole strength relative to phenomenological approximations of the GDR has been found that is similar to the finding in the neighbor ^{138}Ba but less distinctive than that in the odd-mass neighbor ^{139}La.

QRPA calculations describe the gross properties but show strong fluctuations in the GDR region and too little strength at low energy. In the RQTBA calculations, which include 2q⊗phonon excitations, the strength is more fragmented. This fragmentation produces a more smooth shape of the GDR and brings strength to low energy.

ACKNOWLEDGMENTS

We thank A. Hartmann for his technical support. We also thank the crews of the ELBE accelerator and of the HIγS facility for their collaboration during the measurements. The helpful work of E. Birgersson, E. Grosse, and J. Johnson is also acknowledged. We gratefully thank J. Jolie and C. Fransen, University of Cologne, for lending us ^{136}Ba isotopic material. This work was supported by Deutsche Forschungsgemeinschaft, Project No. SCHW883/1-1; the Helmholtz Alliance ExtreMe Matter Institute; and the US Department of Energy, Grants No. DE-FG02-97ER41033 and No. DE-FG02-97ER41042.

[1] F. Voss, K. Wisshak, K. Guber, F. Kappeler, and G. Reffo, Phys. Rev. C **50**, 2582 (1994).
[2] M. Arnould and S. Goriely, Phys. Rep. **384**, 1 (2003).
[3] G. Schramm *et al.*, Phys. Rev. C **85**, 014311 (2012).
[4] M. Salvatores and G. Palmiotti, Prog. Part. Nucl. Phys. **66**, 144 (2011).
[5] P. Axel, Phys. Rev. **126**, 671 (1962).
[6] R. Capote *et al.*, Nucl. Data Sheets **110**, 3107 (2009).
[7] A. R. Junghans *et al.*, Phys. Lett. B **670**, 200 (2008).
[8] A. M. Lane, Ann. Phys. (NY) **63**, 171 (1971).
[9] S. Volz *et al.*, Nucl. Phys. A **779**, 1 (2006).
[10] A. Zilges *et al.*, Phys. Lett. B **542**, 43 (2002).
[11] S. Goriely, Phys. Lett. B **436**, 10 (1998).
[12] E. Litvinova *et al.*, Nucl. Phys. A **823**, 26 (2009).
[13] A. Makinaga *et al.*, Phys. Rev. C **82**, 024314 (2010).
[14] A. Tonchev *et al.*, Phys. Rev. Lett. **104**, 072501 (2010).
[15] D. Savran *et al.*, Phys. Rev. Lett. **100**, 232501 (2008).
[16] N. Pietralla *et al.*, Phys. Rev. C **58**, 796 (1998).
[17] M. Islam *et al.*, Phys. Rev. C **42**, 207 (1990).
[18] R. Chrien *et al.*, Phys. Rev. C **9**, 1622 (1974).
[19] R. Schwengner *et al.*, Nucl. Instrum. Methods Phys. Res. A **555**, 211 (2005).
[20] F. Ajzenberg-Selove, Nucl. Phys. A **506**, 1 (1990).

[21] G. Rusev, A. P. Tonchev, R. Schwengner, C. Sun, W. Tornow, and Y. K. Wu, Phys. Rev. C **79**, 047601 (2009).
[22] H. R. Weller *et al*., Prog. Part. Nucl. Phys. **62**, 257 (2009).
[23] D. R. Hamilton, Phys. Rev. **58**, 122 (1940).
[24] S. Agostinelli *et al*., Nucl. Instrum. Methods Phys. Res. A **506**, 250 (2003).
[25] L. Storm and H. Israel, Nucl. Data Tables **A7**, 565 (1970).
[26] R. Schwengner *et al*., Phys. Rev. C **81**, 054315 (2010).
[27] R. Schwengner *et al*., Phys. Rev. C **76**, 034321 (2007).
[28] G. Rusev *et al*., Phys. Rev. C **77**, 064321 (2008).
[29] R. Schwengner *et al*., Phys. Rev. C **78**, 064314 (2008).
[30] N. Benouaret *et al*., Phys. Rev. C **79**, 014303 (2009).
[31] G. Bartholomew *et al*., Adv. Nucl. Phys. **7**, 229 (1973).
[32] D. Brink, Ph.D. thesis, University of Oxford, 1955 (unpublished).
[33] T. von Egidy and D. Bucurescu, Phys. Rev. C **80**, 054310 (2009).
[34] S.I. Al-Quraishi, S.M. Grimes, T.N. Massey, and D.A. Resler, Phys. Rev. C **67**, 015803 (2003).
[35] C. E. Porter and R. G. Thomas, Phys. Rev. **104**, 483 (1956).
[36] L. I. Schiff, Phys. Rev. **83**, 2 (1951).
[37] P. Ring and P. Schuck, in *The Nuclear Many Body Problem* (Springer, New York, 1980).
[38] H. Beil *et al*., Nucl. Phys. A **172**, 426 (1971).
[39] B. L. Berman, R. E. Pywell, S. S. Dietrich, M. N. Thompson, K. G. McNeill, and J. W. Jury, Phys. Rev. C **36**, 1286 (1987).
[40] F. Dönau, G. Rusev, R. Schwengner, A. R. Junghans, K. D. Schilling, and A. Wagner, Phys. Rev. C **76**, 014317 (2007).
[41] F. Dönau, Phys. Rev. Lett. **94**, 092503 (2005).
[42] E. Litvinova, P. Ring, and V. Tselyaev, Phys. Rev. C **78**, 014312 (2008).
[43] E. Litvinova, P. Ring, and V. Tselyaev, Phys. Rev. Lett. **105**, 022502 (2010).